Bioorganic Chemistry 93 (2019) 103287

Contents lists available at ScienceDirect

Bioorganic Chemistry

journal homepage: www.elsevier.com/locate/bioorg

Aminonaphthalimide hybrids of mitoxantrone and amonafide as anticancer and fluorescent cellular imaging agents

Alex D. Johnson[a], Rodrianne Zammit[b], Jasmine Vella[c], Mario Valentino[c], Joseph A. Buhagiar[b], David C. Magri[a,*]

[a] Department of Chemistry, Faculty of Science, University of Malta, Msida, MSD 2080, Malta
[b] Department of Biology, Faculty of Science, University of Malta, Msida, MSD 2080, Malta
[c] Department of Physiology and Biochemistry, Faculty of Medicine & Surgery, University of Malta, Msida, MSD 2080, Malta

ARTICLE INFO

Keywords:
Aminonaphthalimide
Fluorescence
Mitoxantrone
Amonafide
Cytotoxicity
Apoptosis

ABSTRACT

Novel water-soluble 4-aminonaphthalimides were synthesised and their cellular fluorescent imaging, cytotoxicity and ability to induced apoptosis evaluated. The lead compound **1** was designed from the cross-fertilisation of the basic hydrophilic amino pharmacophore of mitoxantrone, and an aminonaphthalimide scaffold of the drug candidate, amonafide. The compounds are also fluorescent pH probes based on photoinduced electron transfer (PET) and internal charge transfer (ICT). The compounds are sensitive to solvent polarity with large Stoke shifts (> 90 nm) and provide emissive-coloured solutions (blue to yellow). Excited state pK_as of 9.0–9.3 and fluorescence quantum yields of 0.47–0.58 were determined in water. The cytotoxicity and cellular fluorescent imaging properties of the compounds were tested on human cancer cell lines K562 and MCF-7 by the MTT assay, phase contrast and fluorescence microscopy. Compounds **1** and **3** with flexible aminoalkyl chains exhibited GI_{50} comparable to amonafide, while **2** and **4** with a rigid piperazine moiety and butyl chain are less cytotoxic. Fluorescence microscopy with **1** allowed for the visualization of the intracellular microenvironment exemplifying the potential utility of such hybrid molecules as anticancer and fluorescent cellular imaging agents.

1. Introduction

Mitoxantrone (Novantrone™) is a simplified, synthetic analogue of naturally occurring anthracycline antibiotics exemplified by doxorubicin (Fig. 1) [1]. Both drugs are used as antineoplastic agents in the treatment of rapidly proliferating cancers such as acute myeloid leukemia, non-Hodgkin's lymphoma, metastatic breast cancer and prostate cancer [2]. Mitoxantrone is also used as a drug for managing multiple sclerosis [3]. The cytotoxicity of doxorubicin and mitoxantrone is attributed to many different mechanistic pathways [4]. The primary mechanism of action is believed to be as DNA intercalators (with binding preferentially at guanine-cytosine base pairs), and as type II topoisomerase poisons, which form stable DNA-drug-enzyme complexes and trigger apoptosis [5]. A second mechanism of action is the chelation of free iron, which contributes towards the formation of reactive oxygen species, and subsequently generates single-strand DNA fragments [6]. A third mechanism of action is thought to involve the inhibition of helicases, which function to unravel double-stranded DNA into single strand DNA [7]. Structure-activity relationship (SAR) studies have identified a carbonyl and an amino side chain group as essential pharmacophore features [1,5]. The cardiotoxicity of mitoxanthrone, although lower than other naturally occurring analogues including doxorubicin, remains an undesirable side effect [8].

Naphthalimides (benz[*de*]isoquinolin-1,3-diones) are another potentially useful class of anticancer agents, which have been thoroughly reviewed [9–13]. Two drug candidates, amonafide (a 3-amino-1,8-naphthlimide) and mitonafide (a 3-nitro-1,8-naphthalimide) were withdrawn in late stage clinical trials due to unacceptable bone marrow toxicity levels [14]. Elinafide, a symmetrical dimeric *bis*-naphthalimide with two naphthalimide chromophores and a dicationic linker progressed to phase II clinical trials for the treatment of ovarian cancer, and phase I trials for the treatment of various solid tumours, but was discontinued due to its neuromuscular dose-limiting toxicity. While naphthalimides are generally regarded as DNA topoisomerase type II inhibitors, new mechanisms of action are being discovered [10,15].

Current medical research is pursuing a multi-target drug approach

* Corresponding author.
E-mail address: david.magri@um.edu.mt (D.C. Magri).

https://doi.org/10.1016/j.bioorg.2019.103287
Received 3 July 2019; Received in revised form 28 August 2019; Accepted 15 September 2019
Available online 17 September 2019
0045-2068/

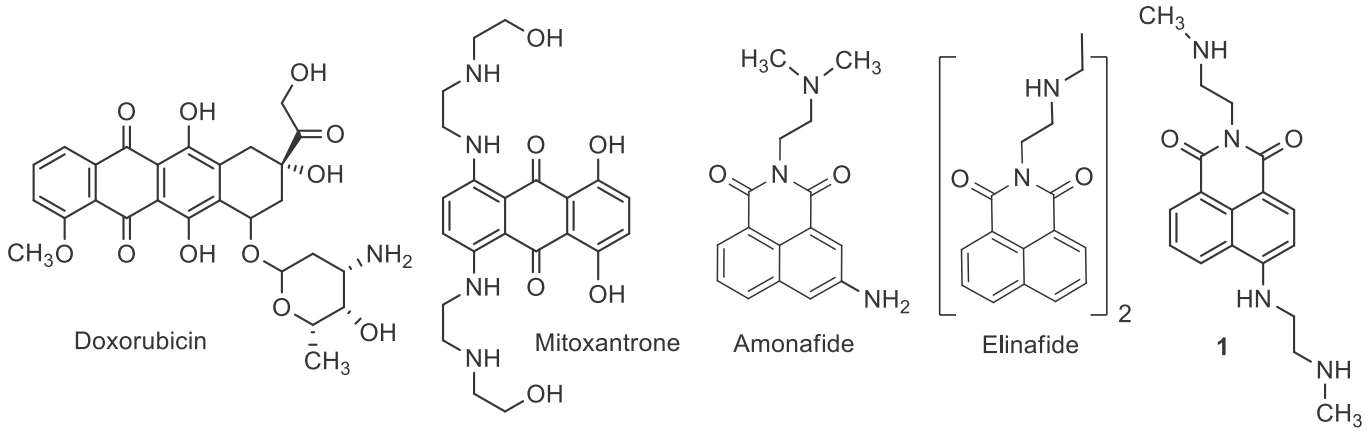

Fig. 1. The chemical structures of anticancer drugs (doxorubicin and mitoxantrone) and naphthalimide-based drug candidates (amonafide and elinafide) and novel compound **1**.

whereby a single chemical entity can modulate several targets associated with a multifactorial disease [16]. For example, studies by Qian reported naphthalimide-cyclam conjugates as multi-target receptor tyrosine kinase inhibitors [17] and naphthalimides with polyamines and long alkyl chains as DNA intercalators and lysosomotropic detergents [18]. SAR studies highlight that an amino-protonable side chain with an ethylene or propylene spacer between the naphthalene ring and the terminal nitrogen atom plays a synergistic effect in increasing DNA binding and inhibition of cancer cell growth [19–21]. At physiological pH these terminal amino chains are protonated, which ensures water solubility and promotes electrostatic interactions with the negatively charge DNA phosphate backbone, thus facilitating intercalation [9].

We hypothesised that cross-fertilization of the naphthalimide scaffold with essential pharmacophore features of mitoxantrone and elinafide might result in promising new anticancer agents with fluorescent cellular imaging properties [11]. Hence, we have synthesised a series of small molecules **1–4** with 4-aminonaphthalimide and at least one aminoethylene or piperazine chain. Aminonaphthalimides have many advantageous physiochemical properties such as large Stokes shifts, long emission wavelengths and high fluorescent quantum yields [22,23], in addition to many advantageous biological properties, such as being cell-permeable, biocompatible, sensitive and site-specific [11]. Studies have demonstrated the selective targeting of aminonaphthalimides for specific organelles including the mitochondria, lysosomes or nuclei within living cells [24–31].

Herein we report the synthesis, characterisation, photophysics and anti-proliferation properties of novel water-soluble derivatives of 4-aminonaphthalimides **1–4** as dual anticancer agents and fluorescent imaging agents. The compounds differ in the side chains at the imide and 4-amino positions. Compounds **1** and **4** possess a *N*-methylethyleneamine and butyl chain, respectively, and **2** and **3** possess methyl groups at the imide end. At the 4-naphthalimide position **2** has a piperazine moiety while the other three compounds have an *N*-methylethyleneamine side chain. The pH dependent fluorescence in aqueous solution and solvent polarity effects were investigated to better understand the intracellular imaging application. The anti-proliferation and fluorescent cellular imaging properties were evaluated on two cancer cells lines, K562 (a myelogenous leukemia) and MCF-7 (human breast cancer). The mode of cell death was delineated by examining the cell morphology by phase contrast microscopy and the cellular uptake properties were examined by fluorescence microscopy.

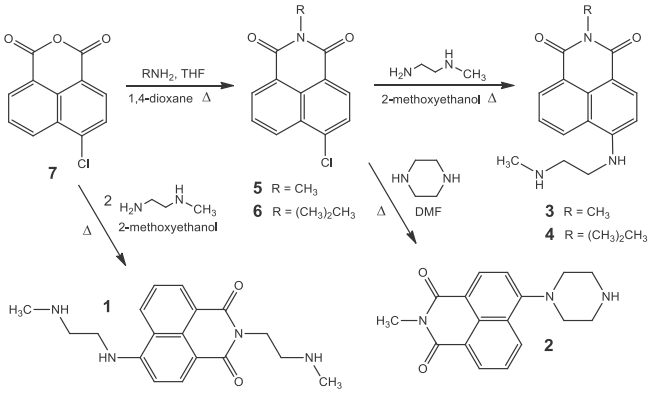

Scheme 1. Synthetic routes of compounds **1–4**.

2. Results and discussion

2.1. Synthesis

The compounds **1–4** were synthesised from 4-chloro-1,8-naphthalic anhydride **7** (Scheme 1). The methylated and butylated precursors, 4-chloro-*N*-methyl-1,8-naphthalimide **5** and 4-chloro-*N*-methyl-1,8-naphthalimide **6** were prepared from methylamine and butylamine in 81% and 76% yield. Compounds **2–4** were subsequently synthesised by nucleophilic aromatic substitution with either piperazine in DMF to yield **2** in 77% yield or *N*-methylethylenediamine in 2-methoxyethanol to give **3** or **4** in 45% and 23% yield, respectively. Doubly aminoalkyl substituted **1** was prepared directly from **7** with excess *N*-methylethylenediamine in 2-methoxyethanol in 80% yield. The coloured solids were characterised by melting point determination, ^{1}H NMR, ^{13}C NMR and FTIR spectroscopy and high resolution mass spectrometry (HRMS) (Figs. S1–S10).

2.2. UV–vis absorption and fluorescence spectroscopic studies

The UV–visible absorption spectra of **1–3** were obtained in water and 1:1 (*v*/*v*) methanol/water (Fig. 2(a–c)) as a function of pH. Photophysical parameters are provided in Table 1. Compound **4** with a butyl rather than a methyl substituent at the *N*-imide position was not studied in solution as the photophysics were expected to be identical to **3**. Compound **3** exhibits a broad absorption band at 447 nm in basic solution and 434 nm in acidic solution. The large magnitudes of ε are

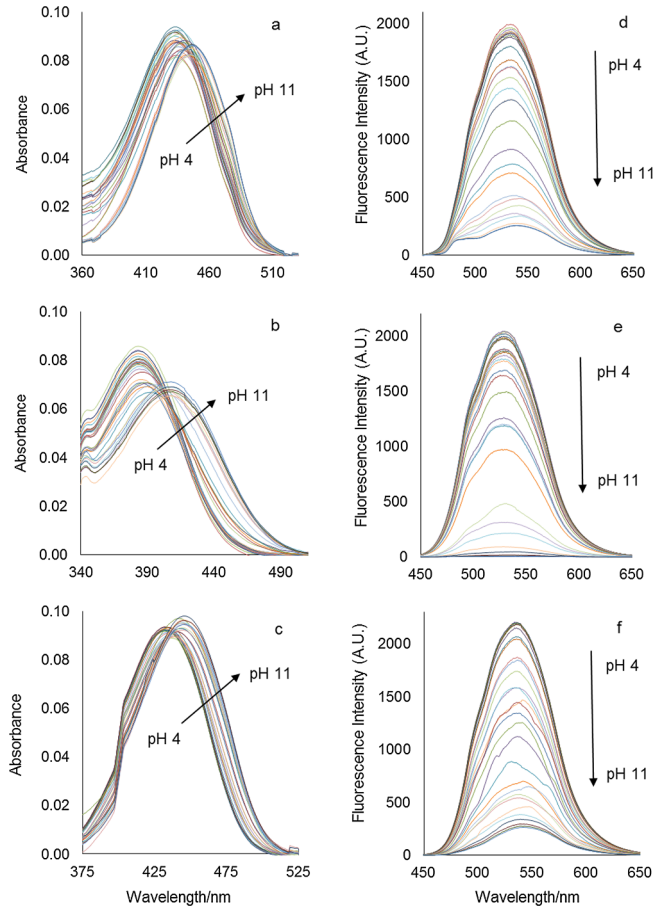

Fig. 2. pH titrations of 9.3 μM **3**, 9.6 μM **2,** and 8.4 μM **1** in 1:1 (*v/v*) MeOH/H_2O; (a–c) UV–visible absorption spectra, and (d–f) fluorescent emission spectra excited at the isosbestic points of 438 nm, 401 nm and 442 nm, respectively for **1–3**.

Table 1
Photophysical data of **1–3** in water and 1:1 (*v/v*) methanol/water by UV–visible absorption and steady-state fluorescence spectroscopy.[a,b]

	1 H_2O	**1** MeOH/H_2O	**2** H_2O	**2** MeOH/H_2O	**3** H_2O	**3** MeOH/H_2O
$\lambda_{Abs\ (pH\ 11)}$/nm	448	445	398	407	447	447
$\lambda_{Abs\ (pH\ 4)}$/nm	434	431	387	384	433	434
λ_{isos}/nm	441	438	393	401	440	442
$\lambda_{Flu\ (pH\ 4)}$/nm	540	535	538	528	538	533
$\Delta\lambda$/nm[d]	99	97	145	127	98	91
pK_a[e]	9.3	8.6	9.0	8.1	9.0	8.5
$\Phi_{Fmax\ (pH\ 4)}$/[f]	0.47	0.26	0.50	0.23	0.58	0.25
$\Phi_{Fmin\ (pH\ 11)}$[f]	0.055	0.033	0.001	0.002	0.046	0.022
FE[g]	8.5	7.8	500	120	13	11

[c]Molar absorptivity ε in L mol^{-1} cm^{-1}.
[a] Sensor concentration ~ 8–10 μM.
[b] Adjusted with CH_3SO_3H and KOH solutions.
[d] Stokes shift $\Delta\lambda = \lambda_{Flu} - \lambda_{Abs}$.
[e] Determined by $\log[(I_{max} - I)/(I - I_{min})] = -\log\ [H^+] + \log\ pK_a$ from fluorescence emission spectra. The slope was unity ± 0.14 with $R^2 > 0.990$.
[f] Relative Φ_{Fmax} with reference to disodium salt of fluorescein in ethanol (0.97). Triplicate experiments with error ± 10%.
[g] Fluorescence enhancement factor [FE = $(I_{max\ pH\ 4})/(I_{max\ pH\ 11})$].

consistent with an π–π* electronic transition. The 13 nm hypsochromic shift is a consequence of a less stable Frank-Condon charge transfer excited state on protonation. Similarly, **1** has absorption bands at 445 nm and 431 nm in basic and acidic solutions, respectively, with a near identical hypsochromic shift of 14 nm in MeOH/H_2O. In water, there is a 3 nm red-shift in the λ_{max} to 448 nm and 434 nm. Isosbestic points are observed in water at 441 nm and 440 nm for **1** and **3**, respectively. The peak maxima of **2** in water are situated to shorter wavelengths of 398 nm and 387 nm in basic and acidic solution with an isosbestic point at 393 nm. In MeOH/H_2O, the corresponding values are 407 nm and 384 nm with an isosbestic point at 401 nm. Noticeably, a more dramatic 23 nm hypsochromic shift and an increase in the peak absorbance are observed on protonation (Fig. 1b).

The compounds function as fluorescent pH probes based on photoinduced electron transfer (PET) and/or internal charge transfer (ICT). The fluorescence emission spectra of **1–3** are shown in Fig. 1(d–f) in 1:1 (*v/v*) methanol/water on excitation at the isosbestic points. Broad emission spectra were obtained with peak maxima at 535 nm, 528 nm and 533 nm for **1**, **2** and **3**, respectively. The large Stokes shift of 91 nm, 127 nm, and 97 nm ensure there is no significant overlap between the absorption and emission spectra. In water, the peak maxima are 5–7 nm larger resulting in greater Stokes shifts. Titration with acid from basic to acidic conditions results in a fluorescent increase due to protonation of the secondary amine at the 4-position, which arrests ICT to the excited fluorophore. The ICT excited state has a positive charge build-up at the 4-amino position, which accelerates charge transfer from the secondary amine (donor) by an attractive electric field effect [32]. At the *N*-imide position a negative charge build-up creates a repulsive electric field, which inhibits electron transfer from the amine to the excited fluorophore.

Titrations resulted in sigmoidal-shaped fluorescence intensity-pH plots within three log units in each case (Fig. S10) [33]. Acid dissociation constants (pK_a) were determined by fitting the fluorescence intensity versus the pH to a linearised Henderson-Hasselbalch

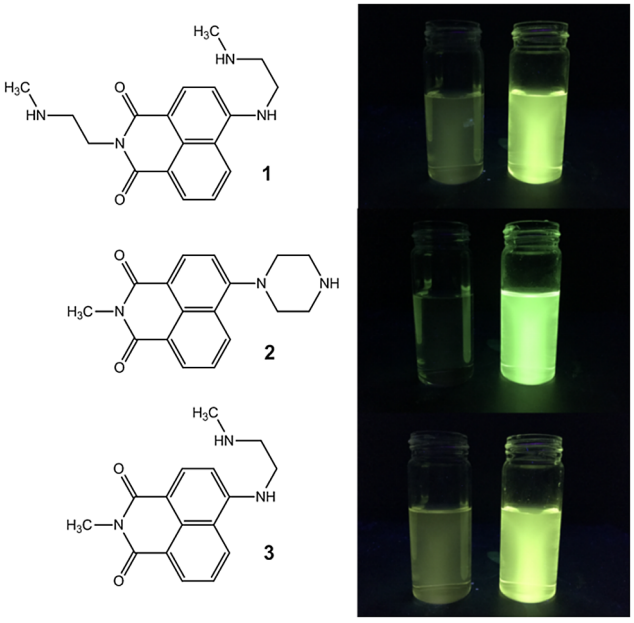

Fig. 3. Compounds **1** (8.4 μM), **2** (9.6 μM) and **3** (9.3 μM) in 1:1 (*v/v*) MeOH/H_2O irradiated with 365 nm UV light from a handheld lamp at pH 11 (left) and pH 4 (right).

expression adapted for spectroscopic measurements according to the equation $pH = pK_a + \log[(I_{max} - I)/(I - I_{min})]$ where the pK_a equals $-\log[H^+]$, I_{max} and I_{min} are the maximum and minimum fluorescence intensities and I is the observed fluorescence intensity as a function of pH. The fits were excellent with a slope of unit and coefficients of determination (R^2) > 0.99. The pK_as in water of **1**, **2** and **3** are 9.3, 9.0 and 9.0 while in 1:1 (*v/v*) methanol/water the pK_as are 8.6, 8.1 and 8.5, respectively [23].

Fig. 3 highlights the bright switching contrast between the 'off' and 'on' states of **1–3**. Compound **2** is superior in terms of the fluorescence switching between the 'off' and 'on' states. No fluorescence is detected from **2** in the 'off' state by the naked eye, which has a fluorescence quantum yields (Φ_F) of 0.001 to 0.002. However, with **1** and **3** the Φ_F are 0.033 and 0.022, which is slightly detectable with the naked eye. On protonation at pH 4 in MeOH/H_2O the Φ_F of **1–3** dramatically increase to about 0.25. In water the Φ_F of **1–3** is significantly brighter between 0.47 and 0.58 [34]. Due to the greater efficiency of the PET/ICT quenching effect in the 'off' state, **2** is the most sensitive with a 120-fold and 500-fold fluorescence enhancements, in MeOH/H_2O and water, respectively. In comparison, **1** and **3** average ratios of 8 and 12, respectively. The efficient charge transfer associated with **2** is due to the greater steric encumbrance of the piperazine, which results in an inherent enhanced twisted ground state [34].

The effect of solvent polarity on the UV–visible absorption and emission spectra of **1** and **3** was investigated after observing a turquoise blue colour on irradiation of a hexane solution of **1** with a 365 nm UV lamp (Table 2). Seventeen solvents were tested with **1**, and 15 solvents with **3**, the latter has very poor solubility in pentane and chloroform. A vibrant range of emission colours were observed for **1** from blue in hexane to orange in water (Fig. 4). The UV–visible absorption spectra of **1** and **3** exhibit broad featureless bands with bathochromic shifts of 55 nm and 22 nm, respectively, from non-polar to polar media, which is characteristic of an π–π* ICT transition. An increase in the solvent polarity generally results in a red shift in the absorption maxima with no significant change in the magnitude of the molar extinction coefficient (log $\varepsilon \sim 4.0 \pm 0.1$).

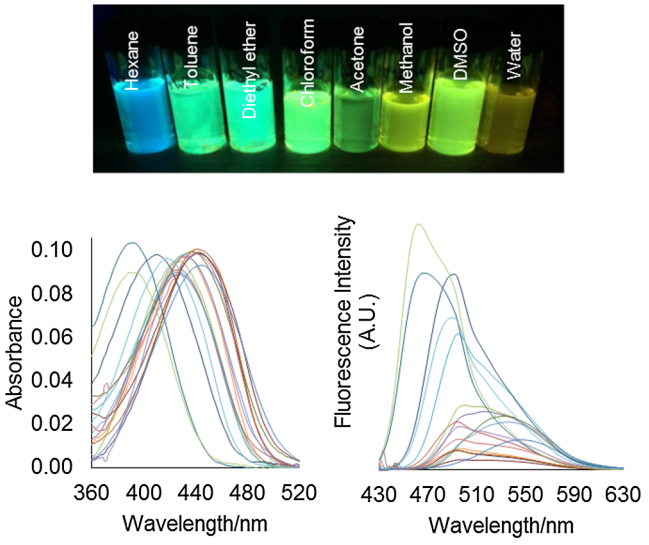

Fig. 4. Neutral solutions of 10^{-5} M **1** irradiated with a 365 nm UV lamp (left to right): hexane, toluene, diethyl ether, chloroform, acetone, methanol, DMSO and water (top). The UV–visible absorption (left) and fluorescent emission (right) spectra of 8.4 μM **1** in various solvents (bottom).

Broad emission bands were observed in all solvents except in the most non-polar solvents, such as pentane and hexane, where some remnants of structured bands appeared. In general, an increase in the solvent polarity resulted in a larger Stokes shift ranging from ~ 60 nm to 100 nm and a decrease in both the fluorescence intensity (and quantum yield). For example, the Stokes shifts of **1** and **3** were 73 nm and 65 nm in toluene, and 101 nm and 107 nm in water, respectively. Protic solvents induce fluorescence quenching by non-radiative hydrogen bonding, from interaction with the 4-amino nitrogen atom and/or a carbonyl oxygen atom.

In Table 2 the fluorescence intensities are tabulated as a ratio with respect to *N, N*-dimethylformamide (DMF), which had the lowest fluorescence intensities. The intensity ratios are greatest in non-polar solvents such as pentane, hexane, diethyl ether, toluene and chloroform with values ranging between 13 and 24. In alcoholic solvents the enhancement factor is typically less than 2. Lippert-Mataga theory was applied to analyse the effect of solvent on the emission spectra (ESI, Fig. S11) [35]. With model **3** a linear regression analysis provided a $R^2 = 0.70$ on analysis of 12 solvents (pentane, hexane, toluene, 1,4-dioxane and chloroform were excluded), while no clear correlation was observed with **1** ($R^2 = 0.03$ excluding hexane and pentane).

2.3. Cytotoxicity studies

The cytotoxicity properties of **1–4** were investigated in K562 (non-adherent myeloid leukaemia) and MCF-7 (adherent human breast cancer) cell lines using the MTT colorimetric assay [36]. The method involves measuring the absorbance at 570 nm of insoluble purple formazan crystals formed after the reduction of the water soluble tetrazolium salt by mitochondrial dehydrogenase enzymes [37]. The cell viability of **1–4** was investigated as a function of concentration (10^{-4}–10^{-8} M) and exposure time (24, 48 and 72 h). An untreated control in the absence of **1–4** was also tested in parallel. The curves involved plotting the absorbance (optical density) as a percentage of the control against concentration (Figs. S12 and S13). The 50% growth inhibition (GI_{50}) of each cell population was determined from the dose-response curves at the point where the curve decreased below the 50% threshold limit.

All compounds **1–4** display some degree of cytotoxicity with GI_{50} values ranging from single to double digit micromolar concentrations (Table 3). The GI_{50} values for each of the three exposure times (24, 48, 72 hrs) represent the average of three independent trials. The optical density was observed to decrease at concentrations above 1 μM (Figs. S12 and S13). Some deviation was observed at all three exposure time intervals for both the K562 and MCF-7 cells where the optical density tended to increase slightly between 0.01 and 1.0 μM from the control. This observation is not uncommon in dose-response studies and may be due to increased cell metabolic activity in response to the agents, notably in the mitochondria [37]. The enhanced metabolic activity of the mitochondria would cause the tetrazolium to be reduced at a faster rate resulting in the formation of more formazan crystals compared to the untreated cells.

The anti-proliferation properties of **1–4** in K562 cells correlate with the compound lipophilicity (log P) at all three time durations. Compound **3** (methyl) exhibits cytotoxicity, while **4** (butyl) is only mildly cytotoxic with an order of magnitude difference in the GI_{50} values. The GI_{50} values of **1** and **3** are comparable to Amonafide ($LC_{50} \sim 12$ μM) [15] and polyamine conjugates alkylated at the naphthalimide imide [38,39]. The anti-proliferation properties of **1–4** with MCF-7 cells are more variable. Compounds **1** and **3** are again the most active: **1** is the most cytotoxic after 24 h of exposure, while **3** is most

Table 2
Photophysical data of **1** and **3** in solvents of different polarity.[a]

		1				**3**		
Solvent	Δf[b]	λ_{Abs}/nm	λ_{Flu}/nm	$\Delta\lambda$/nm	$I_{max\ FE}$[c]	λ_{Abs} /nm	λ_{Flu}[b]/nm	$\Delta\lambda$/nm	$I_{max\ FE}$[c]
Pentane	−0.001	390	462	72	24	–	–	–	–
Hexane	0.001	392	467	75	19	420	458	38	–
Toluene	0.014	417	490	73	15	422	487	65	9.5
1,4-Dioxane	0.022	427	494	67	4.7	423	493	70	11
Chloroform	0.148	426	494	68	13	–	–	–	–
Diethyl ether	0.167	411	491	80	19	422	486	64	13
THF	0.210	433	496	63	4.3	428	497	69	9.4
Dichloromethane	0.218	428	495	67	2.1	430	497	67	9.4
2-Methoxyethanol	0.262	439	495	56	3.0	439	536	97	2.4
DMSO	0.265	437	533	96	5.3	446	540	94	1.5
2-Propanol	0.271	441	494	53	1.9	440	530	90	1.6
DMF	0.276	442	497	55	1.0	439	533	94	1.0
Acetone	0.285	428	500	72	6.3	423	495	72	7.5
Ethanol	0.289	442	494	52	1.9	435	535	100	1.1
Acetonitrile	0.307	428	515	87	5.7	432	521	89	1.9
Methanol	0.309	431	537	106	4.7	436	532	96	1.2
1:1 Methanol/water	0.315	431	535	97	2.6	434	533	91	3.6
Water	0.320	445	546	101	2.9	435	542	107	4.0

[a] Concentration ~ 8 − 10 μM. Excited at λ_{Isos} of 442 nm.
[b] Δf taken from literature data [35].
[c] Fluorescence enhancement ratio with respect to intensity in DMF.

potent after 72 h. Overall, the results are in agreement with reported GI_{50} values with MCF-7 for related alkyl-substituted naphthalimide derivatives (1–30 μM) [19].

2.4. Phase contrast studies

The cytotoxic effect of **1–4** was also investigated by visualising the cells by phase contrast and fluorescence microscopy. Phase contrast images were captured with an Axiovert 40 CLF microscope (Carl Zeiss MicroImaging) to visualise the cell membrane boundary of the K562 and MCF-7 cells. The visible contrast provides insight into the mode of cell death by examination of the shape (and integrity) of the cell membrane. Cell death normally results from either apoptosis (programmed cell death) or necrosis (death by autolysis).

Cells treated with **1–4** were examined after 24, 48 and 72 h and compared to untreated control samples. Phase contrast images of **1** and **3** in K562 and MCF-7 cells are shown in Figs. 5 and S14. The non-adherent K562 cells displayed membrane blebs as small spherical protrusions around the cell membrane after 24 h, which is indicative of apoptosis. After 48 and 72 h, the K562 cells shrink in size and numerous apoptotic bodies are observed. MCF-7 is an adherent cell line. Apoptotic bodies were easily identified after 24 h, although not as prominently as observed with the K562 cell line. The cell membrane forms protrusions that attach to the surface resulting in loss of the adherent properties. After 48 h the MCF-7 cells exhibit membrane protrusions, shrinkage and dislodgement from the surrounding cells. After 72 h, the MCF-7 cells are spherical and no longer stick to the surface. The changes in the cell shape and structure are consistent with apoptosis as the mode of death.

Table 3
In vitro average GI_{50} (50% growth inhibition) values ± SD for **1–4** in K562 and MCF-7.[a,b]

Compound	Log P	24 h	48 h	72 h
		K562 $GI_{50}/\mu M$		
1	0.73	14 ± 0.8	9.0 ± 0.5	6.0 ± 0.7
2	1.65	60 ± 2.9	38 ± 1.2	18 ± 1.0
3	1.10	15 ± 0.8	9.8 ± 0.9	7.8 ± 0.8
4	2.35	94 ± 3.2	84 ± 6.9	79 ± 3.9
		MCF-7 $GI_{50}/\mu M$		
1	0.73	32 ± 2.0	18 ± 1.1	11 ± 0.9
2	1.65	65 ± 5.3	51 ± 4.5	46 ± 3.2
3	1.10	97 ± 6.6	48 ± 2.4	2.2 ± 1.8
4	2.35	–	55 ± 3.9	24 ± 1.9

[a] Values denoted with (–) signify the GI_{50} was not reached within the incubation period or concentration range tested.
[b] MTT assay based on measured absorbance at 562 nm from three independent trials. Standard deviation (SD) error as a range ± 10%. GI_{50} values are averages of three independent trials. Log P values from Chemdraw version 12.0.2.1076.

2.5. Fluorescence imaging in living cells

Fluorescent cell images of K562 and MCF-7 incubated with **1** after 24 h are shown in Fig. 6. The pH of the cytoplasm is ~7.2 so **1** was expected to be protonated and thus fluorescent within the cells [40]. Indeed, nuclei and cytoplasm staining occurs in both cell lines. The greatest contrast was observed inside the nuclei as an intense green fluorescence. Some red fluorescence was also observed in K562 and MCF-7, which was unexpected as red colour was not obtained during the solution studies (Fig. 4). The origin of the red fluorescence is unconfirmed without further study; however, it may be a consequence of intermolecular interactions associated with the inherent push-pull ICT character of the 4-aminonaphthalimide fluorophore [41,42]. Nonetheless, **1** is a novel cytotoxic and fluorescent lead compound for the selective staining and fluorescent imaging of cell nuclei [31].

To better understand the organelle distribution of **1–3**, trials were performed with LysoSensor Green DND-189 and Redox Sensor Red CC-1, commercially available naphthalimide lysosome and rhodamine specific stains [43]. LysoSensor Green DND-189 is cell membrane permeable, and emits a green emission at 540 nm in acidic regions (pK_a = 5.2). While non-fluorescent in the cytosol, it is fluorescent on localisation inside acidic lysosome compartments. Fluorescent images of K562 showed regions of green and red fluorescence within the cytosol, cell membranes and smaller vesicles. Similar results were observed in MCF-7, although the fluorescence intensity was not as vibrant. LysoSensor Green DND-189 gave a weak fluoresce in the nuclei of K562, while no fluorescence was observed in the nuclei of MCF-7 as expected for a non-acidic compartment.

3. Conclusions

In this study, a series of four novel 4-aminonaphthalimides with *N*-

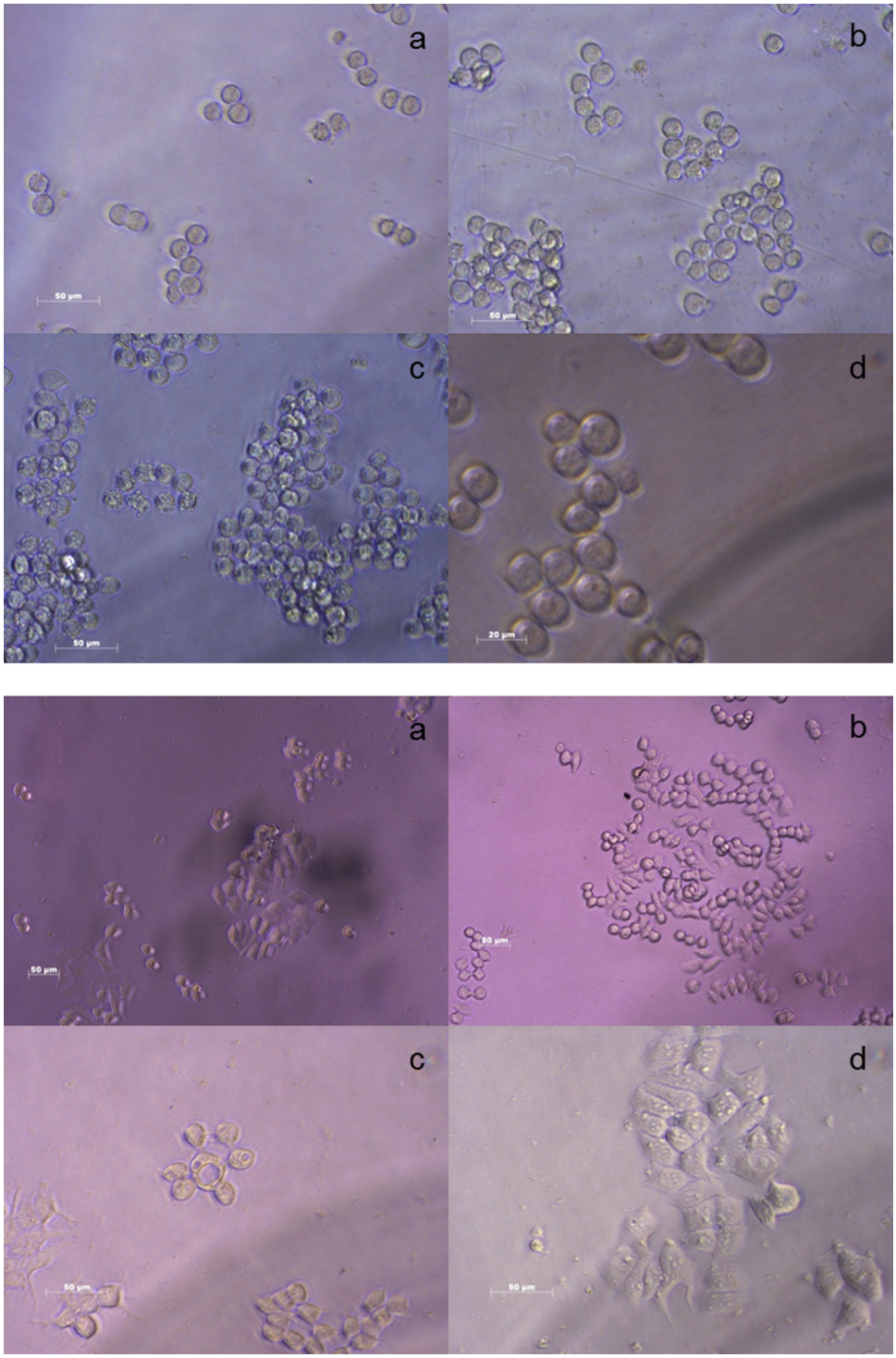

Fig. 5. Phase contrast images at ambient temperature of K562 cells (top) and MCF-7 (bottom) exposed to 150 µM of **1** after 24 hrs (a), 48 hrs (b), 72 hrs (c), and untreated control sample after 72 hrs (d). Scale bar is 50 µm, except for the top right (d), which is 20 µm.

methylethyleneamine or piperazine side chains were synthesised and tested as anticancer and fluorescent cellular imaging agents. The compounds are cell permeable and localise primarily in the nuclei. The greatest cytotoxicity was revealed with the aminonaphthalimide with the two *N*-methylethylene side chains. Besides being water soluble, the compounds are highly fluorescent with solvatochromic properties. Fluorescence is observed in aqueous solution and in the intracellular nuclei of K562 and MCF-7 cells. Phase contrast microscopy and fluorescent staining provide evidence for apoptotic cell death. The results of the study suggest that aminonaphthalimides with secondary alkyl amines are potentially useful cytotoxicity and fluorescent imaging agents.

4. Experimental

4.1. Chemicals

LysoSensor™ Green DND-189 and RedoxSensor™ Red CC-1 were

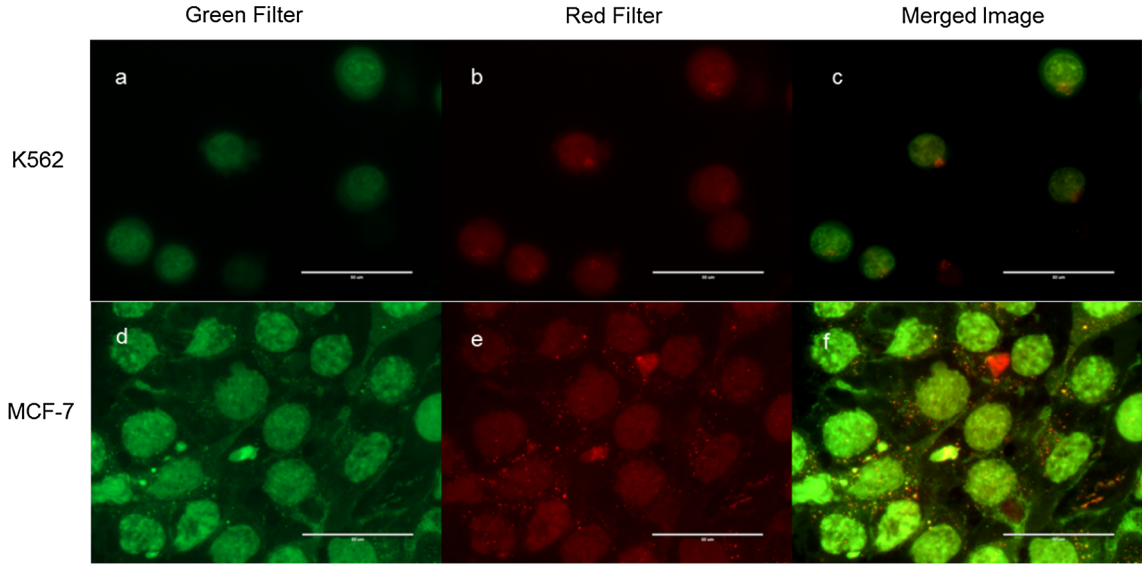

Fig. 6. Fluorescence images at ambient temperature of K562 (a–c) and MCF-7 (d–f) cells incubated at 37 °C stained with 17 μM of **1** after 24 h of exposure. Scale bar of 50 μm.

purchased from Thermo Fisher Scientific. Methyl tetrazolium dye (MTT, 3-(4,5-dimethylthiazol-2-yl)-2,5-diphenyltetrazolium bromide) was purchased from Sigma-Aldrich. Synthetic reagents were purchased from commercial suppliers (Aldrich, Agros) and used as received. Solvents were HPLC grade. Deionised water was used. A comprehensive list of chemicals and suppliers are provided in the ESI.

4.2. Instrumentation

Synthetic reactions were carried in borosilicate round-bottom glassware with IKA C-MAG HS 7 hotplates fitted with an IKA ETS-D5 temperature probe. Thin-layer chromatography (TLC) was conducted on silica gel 60 F_{254} plates visualised with a 254 nm/365 nm handheld UV lamp. Melting points were determined on a Stuart SMP40 automatic melting point apparatus. ^{1}H NMR (500.13 MHz) and ^{13}C NMR (125.76 MHz) spectra were recorded on a Bruker Avance III HD NMR spectrometer (Germany) with chemical shifts reported downfield from TMS at δ = 0.00 ppm and 77.00 ppm for ^{1}H and ^{13}C NMR, respectively. Fourier transform infra-red (FTIR) spectra were recorded with a Shimadzu IR-Affinity-1 spectrophotometer (Japan). High resolution mass spectrometry (HRMS) was performed by Medac Ltd (UK). UV–visible absorption and fluorescence spectra were recorded on a Jasco V-650 spectrophotometer (Japan) and Jasco FP-8300 (Japan) spectrofluorimeter, respectively. Samples were measured in 10 mm diameter (3 mL volume) quartz cuvettes set at medium response, 2 nm bandwidths and scan speed of 200 nm min^{-1}. Excitation and emission slit widths were 2.5 nm and/or 5 nm, respectively. Spectra were background corrected for the solvent. Log P values were obtained from Chemdraw version 12.0.2.1076.

4.3. Chemical synthesis

4.3.1. 4-N-methylethylenediamine-1,8-N-(N-methylethylenediamine) naphthalimide **1**

4-Chloro-1,8-naphthalic anhydride (5.0 g, 22 mmol) and *N*-methylethylenediamine (8 mL) were dissolved in 20 mL of 2-methoxyethanol and refluxed at 120 °C for 24 h. The excess *N*-methylethylenediamine and solvent were removed under vacuum by a rotary evaporator. The crude red oil was washed with ethyl acetate (3 × 20 mL) to give a red solid. Recrystallisation from acetonitrile gave red crystals (5.6 g, 80% yield). R_f = 0.28 (MeOH), m.p. = 198–201 °C; ^{1}H NMR (D_2O, ppm): δ 8.18 (d, 1H, J = 7.4 Hz, Ar—H), 8.15 (d, 1H, J = 8.4 Hz, Ar—H), 8.02 (d, 1H, J = 8.5 Hz, Ar—H), 7.51 (m, 1H, Ar—H), 6.65 (d, 1H, J = 8.6 Hz, Ar—H), 4.32 (t, 2H, J = 5.8 Hz, $-CH_2-$) 3.83 (t, 2H, J = 6.1 Hz, $-CH_2-$), 3.43 (t, 2H, J = 6.1 Hz, $-CH_2-$), 3.35 (t, 2H, J = 5.8 Hz, $-CH_2-$), 2.81 (s, 3H, $-CH_3$), 2.77 (s, 3H, $-CH_3$), The three —NH protons were not observed; ^{13}C NMR (D_2O, ppm): δ 165.5, 164.7, 150.6, 150.6, 134.7, 131.4, 128.7, 124.7, 120.0, 119.6, 107.4, 104.3, 47.9, 47.1, 39.1, 36.7, 33.3, 33.2; IR (KBr, cm^{-1}): 3099, 2959, 1690, 1652, 1587, 1384, 1372; HRMS (ES-ToF): Calculated $C_{18}H_{22}N_4O_2$ $[M + H]^+$ 327.1821, found 327.1819.

4.3.2. 4-N-piperazine-1,8-N-methylnaphthalimide **2**

4-Chloro-*N*-methyl-1,8-naphthalimide (5.0 g, 20 mmol) and excess piperazine (7.4 g, 86 mmol) were dissolved in 20 mL of DMF and refluxed at 120 °C for 5 h. The reaction mixture was extracted with dichloromethane (3 × 20 mL), dried over $MgSO_4$ and gravity filtered. Recrystallisation from ethanol gave a yellow solid (4.6 g, 77% yield). R_f = 0.40 (MeOH), m.p. = 320 °C (dec.); ^{1}H NMR (D_2O, ppm): δ 7.94 (d, 1H, J = 8.3 Hz, Ar—H), 7.68 (d, 1H, J = 7.2 Hz, Ar—H), 7.61 (d, 1H, J = 8.0 Hz, Ar—H), 7.34 (m, 1H, Ar—H), 6.94 (d, 1H, J = 8.1 Hz, Ar—H), 3.59 (br, 4H, $-N(CH_2CH_2)_2N-$), 3.39 (br, 4H, $-N(CH_2CH_2)_2N-$), 2.97 (s, 3H, $-CH_3$), The —NH proton was not observed; ^{13}C NMR (D_2O, ppm): δ 164.1, 163.5, 154.2, 132.0, 130.8, 130.1, 127.2, 125.9, 124.2, 120.0, 115.2, 114.3, 49.4, 44.5, 43.6, 26.3; IR (KBr, cm^{-1}): 3053, 2951, 1687, 1651, 1586, 1383, 1371; HRMS (ES-ToF): Calculated $C_{17}H_{17}N_3O_2$ $[M + H]^+$ 296.1399, found 296.1393.

4.3.3. 4-N-methylethylenediamine-1,8-N-methylnaphthalimide **3**

4-Chloro-*N*-methyl-1,8-naphthalimide (2.0 g, 8.0 mmol) was dissolved in 20 mL of 2-methoxyethanol with excess (2 mL) *N*-methylethylenediamine and refluxed at 120 °C for 24 h. The excess *N*-methylethylenediamine and solvent were removed under vacuum by a rotary evaporator. The crude product was extracted with dichloromethane (3 × 30 mL), dried over $MgSO_4$ and gravity filtered. Recrystallisation from ethanol gave an orange solid (1.0 g, 45% yield). R_f = 0.43 (1:1 (v/v) MeOH/DMSO), m.p. = 127–130 °C; ^{1}H NMR (D_2O, ppm): δ 7.42 (d, 1H, J = 8.0 Hz, Ar—H), 7.25 (d, 1H, J = 7.0 Hz, Ar—H), 7.07 (d, 1H, J = 8.2 Hz, Ar—H), 6.85 (m, 1H, Ar—H), 5.97 (d, 1H, J = 8.5 Hz, Ar—H), 3.40 (t, 2H, J = 6.4 Hz, $-CH_2-$), 3.10 (t, 2H, J = 6.4 Hz, $-CH_2-$), 2.74 (s, 3H, $-CH_3$), 2.65 (s, 3H, $-CH_3$), The two —NH protons were not observed; ^{13}C NMR (DMSO-d_6, ppm): δ 164.0, 163.1, 150.6, 134.1, 130.5, 129.2, 128.5, 124.2, 121.8, 120.1, 107.7, 103.8, 49.2, 42.4, 35.6, 26.3; IR (KBr, cm^{-1}): 3057, 2920, 1695, 1657,

1590, 1388, 1376; HRMS (ES-ToF): Calculated $C_{16}H_{17}N_3O_2$ $[M + H]^+$ 284.1399, found 284.1398.

4.3.4. 4-N-methyl-N,N-ethylenediamine-N-butyl-1,8-naphthalimide **4**

4-Chloro-*N*-butyl-1,8-naphthalimide (1.9 g, 6.6 mmol) was refluxed in excess *N*-methylethylenediamine at 70 °C for 2 h [44]. Dilution with diethyl ether gave a red oil, which was washed with aqueous sodium acetate solution. Recrystallisation from diethyl ether gave a yellow solid (0.49 g, 23% yield). m.p. 69–70 °C; ^{1}H NMR ($CDCl_3$, ppm): δ 8.59 (d, 1H, J = 7.3 Hz, Ar—H), 8.45 (d, 1H, J = 8.4 Hz, Ar—H), 8.16 (d, 1H, J = 8.1 Hz, Ar—H), 7.61 (m, 1H, Ar—H), 6.69 (d, 1H, J = 8.4 Hz, Ar—H), 6.21 (s, 1H, NH), 4.16 (t, 2H, J = 7.5 Hz, $(OC)_2NCH_2$—), 3.43 (m, 2H, —$HNCH_2CH_2NH$—), 3.05 (t, 2H, J = 5.7 Hz, —$HNCH_2CH_2NH$—), 2.52 (s, 3H, –NCH_3), 1.71 (qt, 2H, J = 7.6 Hz, —$NCH_2CH_2CH_2CH_3$), 1.44 (st, 2H, J = 7.4 Hz, —$N(CH_2)_2CH_2CH_3$), 0.97 (t, 3H, 7.4 Hz, -$N(CH_2)_3CH_3$); ^{13}C NMR ($CDCl_3$, ppm): δ 164.8, 164.2, 149.6, 134.5, 131.1, 129.8, 126.3 124.6, 123.2, 120.5, 110.3, 104.4, 49.5, 41.9, 40.0, 35.9, 30.3, 20.5, 13.9; IR ($CHCl_3$, cm^{-1}): 3026, 3011, 2961, 2874, 2857, 1684, 1643, 1582, 1534, 1466, 1431, 1395, 1362, 1242, 1101, 1078; HRMS (ES-ToF): Calculated $C_{19}H_{23}N_3O_2$ $[M + H]^+$ 326.1869, found 326.1876.

4.3.5. 4-Chloro-N-methyl-1,8-naphthalimide **5**

Compound **5** was synthesised as reported [37]. 4-Chloro-1,8-naphthalic anhydride **7** (5.0 g, 21 mmol) was dissolved in 40 mL of 1,4-dioxane and 4 mL of 2 M methylamine in THF and refluxed at 120 °C for 24 h. The solvent was removed under vacuum by a rotary evaporator. Recrystallisation from ethanol gave a yellow solid (4.3 g, 81% yield). R_f = 0.71 (9:1 (v/v) CH_2Cl_2/MeOH); m.p. = 171–173 °C; ^{1}H NMR ($CDCl_3$, ppm): δ 8.68 (d, 1H, J = 7.2 Hz, Ar—H), 8.61 (d, 1H, J = 8.4 Hz, Ar—H), 8.52 (d, 1H, J = 7.8 Hz, Ar—H), 7.86 (m, 1H, Ar—H), 7.84 (d, 1H, J = 7.9 Hz, Ar—H), 3.58 (s, 3H, —CH_3).

4.4. Cell culturing and fluorescence imaging

The K562 and MCF-7 cell cultures were obtained from the European Collection of Authenticated Cell Culture (ECACC). MTT assays were measured using an ELx–808 Bio Tek microplate reader using 96-well plates at 650 nm. Phase contrast images were taken with an Axiovert 40 CLF microscope (Carl Zeiss MicroImaging) with AxioVision Rel. Version 4.8.1 (11–2009) software. Fluorescent images were captured using an EVOS FL Auto Cell Imaging System using an Olympus 40X oil immersion objective and viewed under FITC and rhodamine filters. Rotofix 32A was used as the cytospin for growing the suspension cells (K562) on glass slides.

4.5. MTT cytotoxicity studies

Cells were seeded in 96-well plates at 8000 and 5000 cells/well for K562 and MCF-7, respectively, and incubated at 37 °C for 24, 48, and 72 h at five concentrations between 10^{-4} and 10^{-8} M. After 24 h, each well was treated with a compound and dilution. MTT was prepared by dissolving 1 g in 200 mL of phosphate-buffered saline (PBS) solution. After addition of MTT solution to the 96-wells, cells were incubated for a further 4 h at 37 °C to allow for the formation of formazan crystals. After another 4 h period, the plates were centrifuged for 5 mins at 2500 rpm to fix the cells and formazan crystals to the bottom of the plates. The culture medium was removed by decantation. To each well, 100 µL of DMSO with 25 µL of Sorenson's Glycine Buffer (3.7 g of glycine, 2.9 g NaCl in 500 mL sterile distilled water adjusted to pH 10.5 with NaOH solution) was added. The optical density (absorbance) of each well was measured at 562 nm.

Declaration of Competing Interest

There are no conflicts of interest to declare.

Acknowledgements

The Ministry of The Economy, Investment, and Small Business (MEIB) and the University of Malta are gratefully acknowledged for financial support. The project was supported through the TAKEOFF Seed Fund Award (TOSFA) 2015. Prof. Robert M. Borg is thanked for NMR assistance. Prof. Pierre Schembri-Wismayer is thanked for valuable comments. Stephanie Saliba and Clayton Axiaq are thanked for assistance with the cell culture samples.

Appendix A. Supplementary material

Supplementary data to this article can be found online at https://doi.org/10.1016/j.bioorg.2019.103287.

References

[1] G.L. Patrick, An Introduction to Medicinal Chemistry, fifth ed., Oxford University Press, Oxford, 2013.
[2] R. Marques Damiani, D. Jaqueline Moura, C. Macagnan Viau, R. Andrade Caceres, J. Antonio Pêgas Henriques, J. Saffi, Pathways of cardiac toxicity: comparison between chemotherapeutic drugs doxorubicin and mitoxantrone, Arch. Toxicol. 90 (2016) 2063–2076.
[3] E.J. Fox, Management of worsening multiple sclerosis with mitoxantrone: a review, Clin. Ther. 28 (2006) 461–474.
[4] B.J. Evison, Brad E. Sleebs, K.G. Watson, D.R. Phillips, S.M. Cutts, Mitoxantrone, more than just another topoisomerase II poison, Med. Res. Rev. 36 (2016) 248–299.
[5] B. Pogorelčnik, A. Perdih, T. Solmajer, Recent developments of DNA poisons – human DNA topoisomerase IIα inhibitors – as anticancer agents, Curr. Pharm. Des. 19 (2013) 2474–2488.
[6] E. Tütem, R. Apak, K. Sözgen, The interaction of antitumor-active anthraquinones with biologically important redox couples: I. Spectrophotometric investigation of the interaction of carminic acid and mitoxantrone with the iron(II, III) and copper(I, II) redox couples, J. Inorg. Biochem. 61 (1996) 79–96.
[7] R.K. Zee-Cheng, C.C. Cheng, Antineoplastic agents. Structure-activity relationship study of bis(substituted aminoalkylamino)anthraquinones, J. Med. Chem. 21 (1978) 291–294.
[8] K. Seiter, Toxicity of the topoisomerase II inhibitors, Expert Opin. Drug Saf. 4 (2005) 219–234.
[9] R. Tandon, V. Luxami, H. Kaur, N. Tandon, K. Paul, 1,8-Naphthalimde: a potent DNA intercalator and target for cancer therapy, Chem. Rec. 17 (2017) 956–993.
[10] L. Ingrassia, F. Lefranc, R. Kiss, T. Mitatoric, Naphthalimides and azonafides as promising anti-cancer agents, Curr. Med. Chem. 16 (2009) 1–22.
[11] S. Banerjee, E.B. Veale, C.M. Phelan, S.A. Murphy, G.M. Tocci, L.J. Gillespie, D.O. Frimannsson, J.M. Kelly, T. Gunnlaugsson, Recent advances in the development of 1,8-naphthalimide based DNA targeting binders, anticancer and fluorescent cellular imaging agents, Chem. Soc. Rev. 42 (2013) 1601–1618.
[12] G. Gellerman, Recent developments in the synthesis and applications of anticancer amonafide derivatives, a mini review, Lett. Drug Des. Discov. 13 (2016) 47–63.
[13] M.D. Tomczyk, K.Z. Walczak, 1,8-Naphthalimide based DNA intercalators and anticancer agents. A systematic review from 2007 to 2017, Eur. J. Med. Chem. 159 (2018) 393–422.
[14] M.F. Braña, J.M. Castellano, C.M. Roldán, A. Santos, D. Vázquez, A. Jiménez, Synthesis and mode(s) of action of a new series of imide derivatives of 3-nitro-1,8 naphthalic acid, Cancer Chemother. Pharmacol. 4 (1980) 61–66.
[15] C. Ge, L. Chang, Y. Zhao, C. Chang, X. Xu, H. He, Y. Wang, F. Dai, S. Xie, C. Wang, Design, synthesis and evaluation of naphthalimide derivatives as potential anticancer agents for hepatocellular carcinoma, Molecules 22 (2017) 342, https://doi.org/10.3390/molecules22020342.
[16] Z. Chen, Y. Xu, X. Qian, Naphthalimides and analogues as antitumor agents: A review on molecular design, bioactivity and mechanism of action, Chin. Chem. Lett. 29 (2018) 1741–1756.
[17] S. Tan, K. Han, Q. Li, L. Tong, Y. Yang, Z. Chen, H. Xie, J. Ding, X. Qian, Y. Xu, Novel metal complexes of naphthalimide – cyclam conjugates as potential multitarget receptor tyrosine kinase (RTK) inhibitors: synthesis and biological evaluation, Eur. J. Med. Chem. 85 (2014) 207–214.
[18] Z. Chen, X. Liang, H. Zhang, H. Xie, J. Liu, Y. Xu, A new class of naphthalimide-based antitumor agents that inhibit topoisomerase II and induce lysosomal membrane permeabilization and apoptosis, J. Med. Chem. 53 (2010) 2589–2600.
[19] A. Wu, Y. Xu, X. Qian, J. Wang, J. Liu, Novel naphthalimide derivatives as potential apoptosis-inducing agents: design, synthesis and biological evaluation, Eur. J. Med. Chem. 44 (2009) 4674–4680.
[20] L. Xie, Y. Xu, F. Wang, J. Liu, X. Qian, J. Cui, Synthesis of new amonafide analogues via coupling reaction and their cytotoxic evaluation and DNA-binding studies, Bioorg. Med. Chem. 17 (2009) 804–810.
[21] Z.Y. Tian, S.-Q. Xie, Y.W. Du, Y.-F. Ma, J. Zhao, W.-Y. Gao, C.-J. Wang, Synthesis, cytotoxicity and apoptosis of naphthalimide polyamine conjugates as antitumor agents, Eur. J. Med. Chem. 44 (2009) 393–399.
[22] I. Grabchev, T. Philipopva, P. Meallier, S. Guittonneau, Influence of substituents on the spectroscopic and photochemical properties of naphthalimide derivatives, Dyes.

Pigm. 31 (1996) 31–34.
[23] N.I. Georgiev, V.V. Bakov, V.B. Bojinov, A solid-state-emissive 1,8-naphthalimide probe based on photoinduced electron transfer and aggregation-induced emission, ChemistrySelect 4 (2019) 4163–4167.
[24] L. Wang, M. Fujii, M. Yamaji, H. Okamoto, Fluorescence behaviour of 2-,3- and 4-amino-1,8-naphthalimides: effects of the substitution positions of the amino functionality on the photophysical properties, Photochem. Photobiol. Sci. 17 (2018) 1319–1328.
[25] B. Dong, X. Song, C. Wang, X. Kong, Y. Tang, W. Lin, Dual site-controlled and lysosome-targeted intramolecular charge transfer-photoinduced electron transfer-fluorescence resonance energy transfer fluorescent probe for monitoring pH changes in living cells, Anal. Chem. 88 (2016) 4085–4091.
[26] T. Liu, X. Liu, D.R. Spring, X. Qian, J. Cui, Z. Xu, Quantitatively mapping cellular viscosity with detailed organelle information via a designed PET fluorescent probe, Sci. Rep. 4 (2014) 1–7.
[27] Y. Fu, J. Zhang, H. Wang, J.-L. Chen, P. Zhao, G.-R. Chen, X.-P. He, Intracellular pH sensing and targeted imaging of lysosome by a galactosyl naphthalimide-piperazine probe, Dyes Pigments 133 (2016) 372–379.
[28] J.-T. Hou, W. Xiu Ren, K. Li, J. Seo, A. Sharma, X.-Q. Yu, J.S. Kim, Fluorescent bioimaging of pH: from design to applications, Chem. Soc. Rev. 46 (2017) 2076–2090.
[29] X. Luo, H. Yang, H. Wang, Z. Ye, Z. Zhou, L. Gu, J. Chen, Y. Xiao, X. Liang, X. Qian, Y. Yang, Highly sensitive hill-type small-molecule pH probe that recognizes the reversed pH gradient of cancer cells, Anal. Chem. 90 (2018) 5083–5809.
[30] W. Streciwilk, A. Terenzi, X. Cheng, L. Hager, Y. Dabiri, P. Prochnow, J. Elisabeth Bandow, S. Wölfl, B.K. Keppler, I. Ott, Fluorescent organometallic rhodium(I) and ruthenium(II) metallodrugs with 4-ethylthio-1,8-naphthalimide ligands: anti-proliferative effects, cellular uptake and DNA-interaction, Eur. J. Med. Chem. 156 (2018) 148–161.
[31] J. Zhou, Ana Chang, L. Wang, Y. Liu, X. Liu, D. Shangguan, Effects of side chains on DNA binding, cell permeability, nuclear localization and cytotoxicity of 4-amino-naphthalimides, Org. Biomol. Chem. 12 (2014) 9207–9215.
[32] J.C. Spiteri, S.A. Denisov, G. Jonusauskas, S. Klejna, K. Szacilowski, N.D. McClenaghan, D.C. Magri, Molecular engineering of logic gate types by module rearrangement in 'Pourbaix Sensors': the effect of excited-state electric fields, Org. Biomol. Chem. 16 (2018) 6195–6201.
[33] M.A. Cardona, C.J. Mallia, U. Baisch, D.C. Magri, Water-soluble amino(ethanesulfonate) and [bis(ethanesulfonate)] anthracenes as fluorescent photoinduced electron transfer (PET) pH indicators and Fe^{3+} chemosensors, RSC Adv. 6 (2016) 378–3791.
[34] S. Zheng, P.L.M. Lynch, T.E. Rice, T.S. Moody, H.Q.N. Gunaratne, A.P. de Silva, Structural effects on the pH-dependent fluorescence of naphthalenic derivatives and consequences for sensing/switching, Photochem. Photobiol. Sci. 11 (2011) 1675–1681.
[35] C. Reichardt, Solvatochromic dyes as solvent polarity indicators, Chem. Rev. 94 (1994) 2319–2358.
[36] J. van Meerloo, G.J.L. Kaspers, J. Cloos, Cell sensitivity assays: the MTT assay, in: Ian A. Cree (Ed.), Cancer Cell Culture: Methods and Protocols, second ed. Methods in Molecular Biology, vol. 731, Springer, 2011.
[37] B.G. Campling, J. Pym, H.M. Baker, S.P.C. Cole, Y.M.- Lam, Br. J. Cancer 63 (1991) 75.
[38] F. Dai, H. He, Z. Xu, S. Chen, C. Wang, C. Feng, Z. Tian, H. Dong, S. Xie, Synthesis and biological evaluation of naphthalimide-polyamine conjugates modified by alkylation as anticancer agents through p53 pathway, Bioorg. Chem. 77 (2018) 16–24.
[39] M. Li, Y. Wang, C. Ge, L. Chang, C. Wang, Z. Tian, S. Wang, F. Dai, L. Zhao, S. Xie, Synthesis and biological evaluation of novel alkylated polyamine analogues as potential anticancer agents, Eur. J. Med. Chem. 143 (2018) 1732–1743.
[40] J.-W. Chen, C.-M. Chen, C.-C. Chang, A fluorescent pH probe for acidic organelles in living cells, Org. Biomol. Chem. 15 (2017) 7936–7943.
[41] H.-H. Lin, Y.-C. Chan, J.-W. Chen, C.-C. Chang, Aggregation-induced emission enhancement characteristics of naphthalimide derivatives and their applications in cell imaging, J. Mater. Chem. 21 (2011) 3170–3177.
[42] L. He, B. Dong, Y. Liu, W. Lin, Fluorescent chemosensors manipulated by dual/triple interplaying sensing mechanisms, Chem. Soc. Rev. 45 (2016) 6449–6461.
[43] I. Johnson, M.T.Z. Spence, The Molecular Probes Handbook: A Guide to Fluorescent Probes and Labeling Technologies, 11th ed., Life Technologies Corporation, U.S., 2010.
[44] A.D. Johnson, K.A. Paterson, J.C. Spiteri, S.A. Denisov, G. Jonusauskas, A. Tron, N.D. McClenaghan, D.C. Magri, Water-soluble naphthalimide-based 'Pourbaix sensors': pH and redox-activated fluorescent AND logic gates based on photoinduced electron transfer, New J. Chem. 40 (2016) 9917–9922.